Xiangmeng Meng, Marcel Bachmann, Antoni Artinov, Michael Rethmeier

The influence of magnetic field orientation on metal mixing in electromagnetic stirring enhanced wire feed laser beam welding

Citation details
Meng, X., Bachmann, M., Artinov, A., Rethmeier, M. (2021). The influence of magnetic field orientation on metal mixing in electromagnetic stirring enhanced wire feed laser beam welding. Journal of Materials Processing Technology, 294, 117135. https://doi.org/10.1016/j.jmatprotec.2021.117135.

The influence of magnetic field orientation on metal mixing in electromagnetic stirring enhanced wire feed laser beam welding

Xiangmeng Meng[a,*], Marcel Bachmann[a], Antoni Artinov[a], Michael Rethmeier[b,a]

[a] BAM Federal Institute for Materials Research and Testing, Unter den Eichen 87, 12205 Berlin, Germany

[b] Technische Universität Berlin, Institute of Machine Tools and Factory Management, Pascalstraße 8-9, 10587 Berlin, Germany

Corresponding author: xiangmeng.meng@bam.de

Abstract

The application of the electromagnetic stirring from an oscillating magnetic field can improve the metal mixing in wire feed laser beam welding. However, the extra parameters introduced in this technique make the selection of an optimal combination of process parameters more difficult. In the current study, besides the commonly concerned magnetic flux density and frequency, the influence of the magnetic field orientation (magnetic field angle) on the transport of filler metal is studied numerically and experimentally. *Ex-situ* X-ray fluorescence spectrometer measurements are used to map the metal mixing in the final weld. A three-dimensional transient multi-physical model is developed to reveal the deeper physical essence, considering the coupling between heat transfer, fluid flow, keyhole dynamics, element transport and magnetohydrodynamics. The spatial distribution of the laser energy on the keyhole wall is calculated by a ray tracing algorithm. The results show that the magnetic field with smaller angle with respect to the transverse direction provides better penetration capacity, and its stirring effect can reach the lower part of the molten pool. Therefore, the smaller magnetic field angle produces better metal mixing. A constant downward flow is formed at the lower part of the molten pool when magnetic field of 10° angle is applied, which brings the filler metal to the root region. As the magnetic field angle increases to 40°, the beneficial downward flow changes into a constant upward flow, resulting in a concentration of the filler metal in the upper region. This study provides further insight of the underlying physics in the electromagnetically enhanced laser beam welding, which may guide the optimization of parameters to achieve property homogeneity or to avoid potential defects.

Keywords: laser welding, metal mixing, magnetic field, magnetohydrodynamics, multi-physical modelling

1. Introduction

The deep penetration laser beam welding (LBW) has shown more and more industrial

applications since the rapid development of high power and high beam quality laser sources. However, the typical autogenous LBW still has several limitations in practical application, e.g. the strict requirement for the gap tolerance due to the small size of the laser spot and a possible loss of important alloying elements due to severe metal evaporation.

These limitations can be overcome by a modification of LBW named as wire feed laser beam welding (WFLBW), in which the filler wire is melted by the laser energy and then transferred into the molten pool. The gap bridging capacity can be significantly improved by the melted filler metal. Furthermore, appropriate alloying elements can be added into the molten pool to control the metallurgical behavior if necessary (Torkamany et al., 2015). However, it has also been reported that insufficient metal mixing is a common issue in the WFLBW, especially for thick components. The filler material may concentrate at the upper part of the weld, which is caused by the steep shape of the molten pool and the high cooling rate. The non-uniform element distribution may undermine the mechanical and metallurgical properties or even cause defects, e.g. hot-cracking in the WFLBW of Al alloy.

In the last two decades, more attentions have been drawn to electromagnetic techniques to enhance the traditional LBW process. An induced eddy current can be produced in the electrically conducting molten pool by applying an external magnetic field. This eddy current and the magnetic field itself will generate a volumetric Lorentz force (Moreau, 2013). The relationship between the magnetic field and the Lorentz force can be written as:

$$\vec{F}_L = \vec{j} \times \vec{B} = \sigma_e \left(\vec{v} \times \vec{B} + \vec{E} \right) \times \vec{B} \quad (1)$$

The Lorentz force has two components. One comes from the $\vec{v} \times \vec{B}$ term and is always opposite to the flowing direction of the liquid metal, also known as electromagnetic braking or Hartmann effect. When a transient magnetic field is applied, another component will be generated by the electric field $\vec{E}$ which is induced by the temporal variation of the magnetic field. By applying a magnetic field with proper strength, frequency and orientation, desirable effects such as acceleration, deceleration, supporting or stirring can be produced purposefully to alter the molten pool behavior.

A beneficial effect of an external magnetic field on LBW was found by Kern et al. (2000), in which the molten pool was stabilized to suppress the humping defects forming at high welding speed. Avilov et al. (2016) and Xu et al. (2020) suggested that a transverse oscillating magnetic field applied at the bottom of the workpiece provided an effective support against the metallostatic pressure during full penetration LBW of steel plates up to 20 mm thickness or Al plates up to 10 mm thickness. Similar results were also obtained for the full penetration LBW of Al alloy with a steady magnetic field of 200 mT (Chen et al., 2017). In the work of Fritzsche et al. (2018), a transverse oscillating

magnetic field in the kilohertz range was employed to a partial penetration LBW of Al. More than 70 % porosity reduction, as well as an evident surface stabilization, was achieved.

It has also been confirmed experimentally that an external magnetic field can be used to enhance the mixing of the filler metal in LBW. Gatzen (2012) applied a low-frequency coaxial alternating magnetic field (below 25 Hz) to the molten pool of WFLBW of Al alloy. The Si from the filler wire was significantly homogenized by the electromagnetic stirring (EMS) in the molten pool. In the hybrid laser-arc welding (HLAW), even if the molten filler metal can be accelerated into a much higher downward velocity by the gas metal arc, the filler metal still concentrated at the upper part of the weld. Üstündag et al. (2019) found that the metal mixing in the HLAW of mild steel was radically improved by applying an oscillating magnetic field. In the authors' previous research, a transverse oscillating magnetic field was imposed at the top side of the workpiece during WFLBW of austenitic steel. The additional element was transferred to the root of the molten pool under the downward Lorentz force, and the depth of the well-mixed region was almost doubled (Meng et al. 2019a).

Besides the macro beneficial effect, the weld microstructure can be improved by an external magnetic field. The studies of Xu et al. (2020) and Meng et al. (2019a) suggested that the weld grain structure from LBW of steel or Al alloy can be refined by the mechanical stirring of the Lorentz force when an oscillating magnetic field was applied. Meanwhile, the micro solidification cracking susceptibility was also reduced by the EMS. The steady magnetic field was also found to show beneficial effect on the grain refinement due to the presence of the thermoelectric magnetic convection (Chen et al., 2020). Yan et al. (2019) found that the brittle intermetallic compounds in LBW of steel to Aluminum were suppressed under the influence of a steady magnetic field. The element diffusion was mitigated, and more ductile Fe-rich intermetallic compounds were formed at the interface.

Although many experimental successes have been made to improve the LBW with external magnetic field, only a few experimental investigations on the molten pool behaviors in LBW under magnetic field are available so far, e.g. the metal/glass observation from Rong et al. (2017) and *in-situ* X-ray measurement from Gatzen et al. (2011c). It is partially due to the difficulties in the direct measurement of the molten pool which is non-transparent and is covered by bright vapor plume. Additionally, the highly nonlinear and multi-coupled interactions between the molten pool and the magnetic field make the quantitative analysis more difficult.

To provide a deeper insight into the physical essence of the LBW with magnetic field, some modelling efforts have been made, in which the multi-physical coupling between the thermo-fluid

and the magnetic field, namely magnetohydrodynamics (MHD), was taken into consideration. A 3D steady-state CFD model with fixed keyhole geometry was developed by Bachmann et al. (2014) for the autogenous LBW with a magnetic field. The influences of both steady and oscillating magnetic fields on the molten pool behavior during LBW of non-ferromagnetic materials, e.g. Al and austenitic steel, were studied. Later, they further improved the material model to calculate the thermo-fluid flow in the molten pool of ferromagnetic duplex stainless steel (Bachmann et al. 2016). Chen et al. (2018a) numerically investigated the influence of different orientations of a steady magnetic field on the molten pool dynamics in LBW of Al. This model was then sophisticated to study the induced thermoelectric currents and thermoelectric-magnetic effects (Chen et al., 2018b). However, the keyhole remained predefined in these simulations, neglecting the underlying impacts from the fluctuating keyhole. Recently, self-consistent multi-physical models considering a dynamic keyhole were built by Chen et al. (2019) and Cao et al. (2020) to calculate the molten pool behavior and the thermoelectric current during LBW with steady magnetic field.

Gatzen et al. (2011a) attempted to explain the enhancement of metal mixing in WFLBW with a coaxial magnetic field numerically. The calculated results showed that the periodic EMS produced in the molten pool gave a significant influence on the melt flow pattern and determined the resultant element distribution. However, the keyhole profile in this study was fixed for simplification. In the authors' recent work, a more comprehensive multi-physical model was developed for the electromagnetic stirring enhanced wire feed laser beam welding (EMS-WFLBW), in which the heat transfer, fluid flow, element transport, keyhole dynamics and MHD were all considered self-consistently (Meng et al. 2019b). The molten pool behaviors with and without magnetic field were compared in detail to obtain an intuitive explanation to the benefits on the filler metal mixing from an EMS.

Considering that many new parameters are introduced in this new technique, the selection of the optimal parameters becomes more challenging. Besides the commonly concerned magnetic flux density and frequency, the paper hereby provides a parametric study on the influence of magnetic field orientation (magnetic field angle) on the transport of filler material in the EMS-WFLBW, using numerical modelling and fundamental experiments. The electromagnetic phenomena, e.g. eddy current and Lorentz force, combined with the thermo-fluid flow, the keyhole dynamics and the element transport are calculated by a 3D transient multi-physical model. The model is well verified by the final weld shape and the element distribution measured by an X-ray fluorescence spectrometer (XRF). The different molten pool dynamics under different magnetic field orientations are compared and analyzed.

2. Experimental setup

304 austenitic stainless steel and NiCr20Mo15 alloy were used as the base metal and the filler metal, respectively. The base metal was 200 mm × 60 mm × 10 mm in dimension, and the filler wire was 1.2 mm in diameter. Table 1 gives the nominal compositions of the two materials. Since the base metal and the filler metal have distinct Ni contents, the Ni distribution was measured to characterize the metal mixing in the molten pool.

Table 1 Nominal composition of 304 steel and NiCr20Mo15 alloy (wt.%)

Alloy	Ni	Cr	Mo	Nb	C	Si	S	Fe
304 steel	8.0-10.0	17.5-19.0	-	-	<0.07	<0.75	<0.015	bal.
NiCr20Mo15	bal.	20.0	15	-	0.015	0.1	-	<1.0

An IPG fiber laser system with a maximum 20 kW output and 1070 nm wavelength was used. The laser beam had a diameter of 520 μm at the focal plane which was set 3 mm below the top surface of the base metal during welding. The optical axis of the laser beam was vertical to the top surface of the base metal. A butt joint configuration was performed with a technical zero gap. The laser power was set to 6.5 kW and the welding speed was 1.3 m/min. The filler wire had a leading position with a 57° angle with respect to the optical axis, and the wire feeding speed was 2.1 m/min. Pure Argon was provided behind the laser spot to protect the weld seam from oxidation.

An in-house developed alternating current (AC) electromagnet was used to produce the external magnetic field, see Fig. 1(a). The magnet pole had a cross-section of 16 mm × 16 mm, and the distance between the two magnet poles was set to 20 mm to guarantee a sufficient magnetic flux density. The electromagnet was installed 2 mm above the base metal. The experimental set up is shown in Fig. 1(b). The applicable magnetic field angle was limited in the current experimental circumstance owing to the geometry of the electromagnet, especially the necessarily small distance between the poles of the magnet. The angle of the magnet poles with respect to the y-direction (transverse direction) varied from 10° to 40° in different experimental cases to study the influence of the magnetic field orientation. The electromagnet produced an oscillating magnetic field with a maximum magnetic flux density of 250 mT at a frequency of 3575 Hz. The spatial distribution of the magnetic flux density (denoted as $\vec{B}_0$) which was measured by a Hall sensor in the cold metal testing is plotted in Fig. 2.

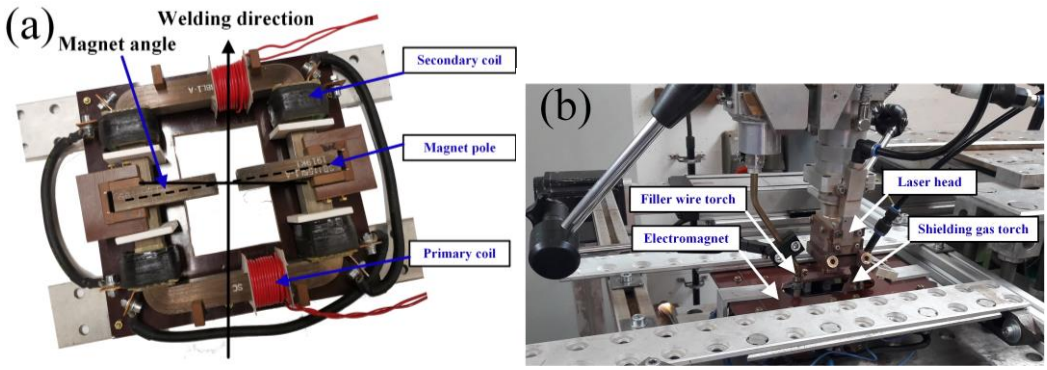

Fig. 1 EMS-WFLBW experiment system: (a) experimental setup, (b) schematic of the magnetic field orientation

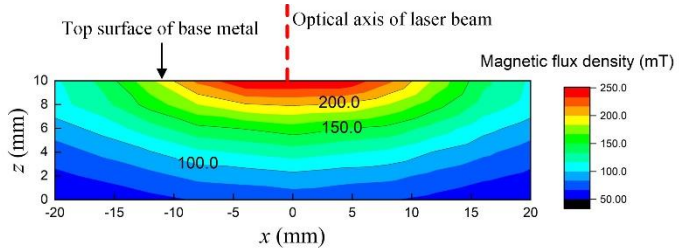

Fig. 2 Experimentally measured external magnetic field $\vec{B}_0$

The weld specimen was mechanically cut, grinded and polished on the cross-section, and then etched by a V2A etchant (100 ml H_2O, 100 ml HNO_3 and 10 ml HCl). An optical microscope was used to observe the fusion line shape on the cross-section. XRF mapping was performed to measure the Ni content on the cross-section to characterize the metal mixing. The scanning spot size was 20 µm and the measurement time per spot was 50 ms, which achieved an accuracy of ± 2 wt. %.

3. Mathematical modelling

A 3D CFD model coupled with MHD and volume-of-fluid (VOF) algorithm is developed in this paper to calculate the heat transfer, fluid flow, free surface deformation, element distribution as well as the electromagnetic behavior during EMS-WFLBW. The mathematical formulations of the numerical model will be given concisely, focusing on the key physical features of the EMS-WFLBW. More detailed descriptions of the simplifications and assumptions, governing equations, boundary conditions, mesh geometry and algorithm can be found in the authors' previous works (Meng et al., 2020). The nomenclatures are summarized in Table 2.

Table 2 Nomenclatures

Symbol	Nomenclature	Symbol	Nomenclature
A, B	Evaporation coefficients	S_q	Heat source term
$\vec{B}_0$	Externally imposed magnetic field	$\vec{S}_{\mathbf{m}}$	Momentum source term
$\vec{b}$	Secondarily induced magnetic field from temporal variation of $\vec{B}_0$ and liquid flow	S_{Ni}	Element source term from filler wire
w_{Ni}	Weight percentage of Ni	$\vec{s}$	Tangential vector
c_{p}	Specific heat	t	Time
D_{Ni}	Diffusion coefficient of Ni in iron	T	Temperature
f	Frequency	T_{S}, T_{L}	Solidus and liquidus temperature
F	Volume fraction	T_0	Ambient temperature
$\vec{F}_L$	Vector of Lorentz force	T_{w}	Temperature of liquid filler metal
F_{s}	Volume fraction of steel	v_{evp}	Evaporation recession speed of the free surface
$\vec{g}$	Vector of gravity acceleration	$\vec{v}$	Velocity vector
h_{c}	Convection heat transfer coefficient	v_{n}	Normal velocity
h	Enthalpy	v_{t}	Tangential velocity
h_{w}	Energy source from the liquid filler metal	v_{speed}	Welding speed
$\vec{I}$	Vector of the incident ray	$\vec{v}_w$	Velocity vector of the liquid filler metal
$\vec{j}$	Current density	x, y, z	Coordinates
k	Thermal conductivity	z_0	Position of focal plane
K	Carman–Kozeny equation coefficient	z_{r}	Rayleigh length
k_{b}	Boltzmann constant	α	Absorbance
k_{l}	Entropy factor	β	Expansion coefficient
m_{a}	Molar mass	δ	Skin depth
m_{w}	Mass source from the filler wire	ΔL_{v}	Evaporation latent heat
$\vec{n}$	Normal vector	ΔH_{w}	Melting latent heat of the filler metal
N_{a}	Avogadro constant	γ	Surface tension
p	Hydrodynamic pressure	ε_{r}	Emissivity
p_{ca}	Capillary pressure	ε	Material-dependent coefficient (0.25)
p_r	Recoil pressure	θ	Incident angle
p_{vapor}	Stagnation pressure of the metal vapor	κ	Curvature
P_{L}	Laser power	μ	Dynamic viscosity
q_{L}	Laser energy density	μ_{m}	Permeability
q_{plume}	Heat flux from the high-temperature plume	ρ	Density
q_{recond}	Heat flux from the metal vapor's re-condensation	ρ_{s}	Density of steel

r_w	Radius of the filler wire	σ	Stefan-Boltzmann constant
r_f	Laser beam radius	σ_e	Electrical conductivity
r_{f0}	Laser beam radius at the focal plane	τ_{ma}	Marangoni stress
$\vec{R}$	Vector of the reflected ray	τ_{vapor}	Shear stress of the metal vapor
R_g	Ideal gas constant		
S_F	Volume source from the filler wire		

3.1 Governing equations

- Mass conservation equation

$$\nabla \cdot \vec{v} = \frac{m_w}{\rho} \quad (2)$$

- Momentum equation

$$\rho\left(\frac{\partial \vec{v}}{\partial t} + \vec{v} \cdot \nabla \vec{v}\right) = -\nabla p + \mu \nabla^2 \vec{v} - \mu K \vec{v} + m_w \vec{v}_w + \vec{S}_m \quad (3)$$

- Energy equation

$$\rho\left[\frac{\partial h}{\partial t} + (\vec{v} \cdot \nabla) h\right] = \nabla \cdot (k \nabla T) + h_w + S_q \quad (4)$$

- VOF equation

$$\frac{\partial F}{\partial t} + \nabla \cdot (\vec{v} F) = S_F \quad (5)$$

- Magnetic induction equation

$$\frac{\partial \vec{b}}{\partial t} + (\vec{v} \cdot \nabla)\vec{b} = \frac{1}{\mu_m \sigma_e} \nabla^2 \vec{b} + \left((\vec{B}_0 + \vec{b}) \cdot \nabla\right)\vec{v} - (\vec{v} \cdot \nabla)\vec{B}_0 \quad (6)$$

It is assumed that the solidified weld bead perfectly maintains austenitic microstructure, and therefore μ_m is equal to 1 in the whole simulation domain. In order to reduce the computational intensity to an acceptable level, the AC electromagnet which is the source of the external magnetic field is excluded from the model. Instead, the $\vec{B}_0$ from Fig. 2 is taken as input data, moving with the laser spot during calculation.

- Ni transport equation

$$\frac{\partial F_s \rho_s w_{Ni}}{\partial t} + \nabla \cdot \left(F_s \rho_s \vec{v} w_{Ni} - F_s D_{Ni} \nabla w_{Ni} \right) = S_{Ni} \quad (7)$$

3.2 Physical models in EMS-WFLBW

When a proper position and angle of the filler wire are selected, the filler wire will be melted by a part of the laser beam. The melted filler metal flows downward into the molten pool in the form of a continuous liquid bridge or discontinuous droplets. A liquid bridge transfer has been confirmed by the high-speed imaging in the authors' previous study (Meng et al., 2019a). Meanwhile, a part of the laser beam may also be reflected from the melting front of the filler wire into the atmosphere, resulting into energy dissipation. The interaction between the filler wire and the laser beam is not simulated in the model, instead, the temperature and the velocity of the liquid bridge are taken from the available experimental and numerical studies. According to the measurement of Arata et al. (1986), the efficiency of the absorbed laser energy on the melting front of the filler wire is about 7.2%, and the average temperature of the liquid bridge can reach up to 2900 K. The velocity of the liquid filler metal is taken as 0.5 m/s from the numerical work of Hu et al. (2019).

It is assumed that the energy density of the laser beam has an ideal Gaussian distribution at an arbitrary horizontal plane, which gives

$$q_L(x, y) = \frac{2P_L}{\pi r_f^2} \exp\left(-2 \frac{x^2 + y^2}{r_f^2} \right) . \quad (8)$$

Part of the laser beam is blocked out (absorbed or reflected) by the filler wire before it reaches the workpiece surface, as shown in Fig. 3(a).

A self-consistent ray tracing algorithm is implemented to describe the spatial distribution of the laser energy on the keyhole wall (Cho et al., 2012). Firstly, the laser beam is discretized into more than 1000 sub-rays, and each sub-ray has its own location-dependent energy density, as shown in Fig. 3(a). The initial direction of the sub-ray ($\vec{I}_0$) at the discretization plane is determined by the diffraction feature of the laser beam, which can be expressed by the variation of the beam radius along the optical axis:

$$r_f(z) = r_{f0} \left[1 + \left(\frac{z - z_0}{z_r} \right)^2 \right]^{1/2} . \quad (9)$$

Subsequently, the multiple reflections of all sub-rays and the Fresnel absorption at every reflection position are calculated, as shown in Fig.3(b). The direction of the *i*-th reflection ($\vec{R}_i$) is determined by the *i*-th incident direction $\vec{I}_n$ and the normal vector ($\vec{n}_i$) at the *i*-th reflection point. The $\vec{R}_i$ can be then taken as the (*i*+1)-th incident direction $\vec{I}_{i+1}$ for the following reflections until the sub-ray escapes from the simulation domain or the energy density reduces to a certain value.

$$\vec{R}_i = \vec{I}_{i+1} = \vec{I}_i - 2\left(\vec{I}_i \cdot \vec{n}_i\right)\vec{n}_i \quad i = 0,1,2\ldots \quad .(10)$$

The Fresnel reflection model is adopted to calculate the absorption rate at every reflection position (Schulz et al., 1987):

$$\alpha = 1 - \frac{1}{2}\left(\frac{1+\left(1-\varepsilon\cos\theta_i\right)^2}{1+\left(1+\varepsilon\cos\theta_i\right)^2} + \frac{\varepsilon^2 - 2\varepsilon\cos\theta_i + 2\cos^2\theta_i}{\varepsilon^2 + 2\varepsilon\cos\theta_i + 2\cos^2\theta_i}\right). \quad (11)$$

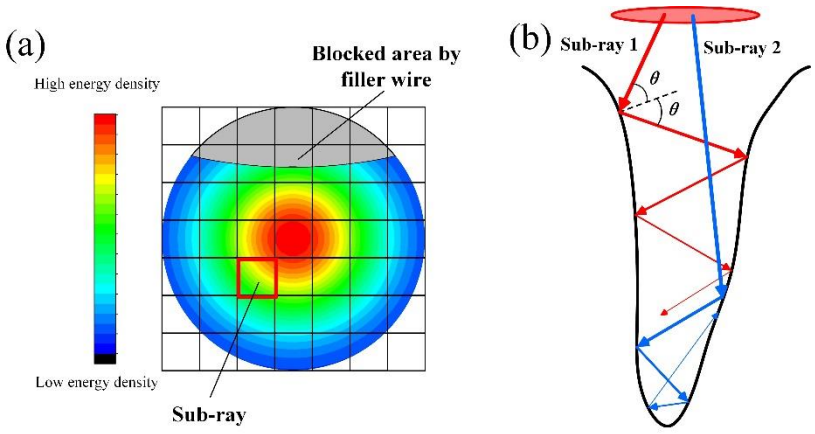

Fig. 3 Ray tracing algorithm: (a) discretization of the laser beam energy; (b) multiple reflections on the keyhole wall

The predominant driving force for the keyhole formation is the recoil pressure due to metal evaporation. Its magnitude is calculated by the following analytical equation (Semak and Matsunawa, 1997):

$$p_r = \frac{AB}{\sqrt{T}}\exp\left(-\frac{m_a \Delta L_v}{R_g T}\right). \quad (12)$$

The effects of the temperature-dependent surface tension result into two components: the capillary pressure in the normal direction to the free surface and the Marangoni stress in the tangential direction, as shown below:

$$p_{ca} = \gamma\kappa \quad (13)$$

$$\tau_{\mathrm{ma}} = \frac{\partial \gamma}{\partial T}\frac{\partial T}{\partial \vec{s}} \text{ . (14)}$$

The volumetric forces involved in the EMS-WFLBW include the hydrostatics pressure, buoyancy and induced Lorentz force which can be calculated as follows:

$$\vec{F}_{\mathrm{h}} = \rho \vec{g} \quad (15)$$

$$\vec{F}_{\mathrm{b}} = -\beta\rho(T - T_{\mathrm{L}})\vec{g} \quad (16)$$

$$\vec{F}_{\mathrm{L}} = \vec{j} \times \vec{B} = \frac{1}{\mu_m}\nabla \times \left(\vec{B}_0 + \vec{b}\right) \times \left(\vec{B}_0 + \vec{b}\right) \quad (17)$$

These volumetric forces are implemented into the source term $\vec{S}_{\mathrm{m}}$ in Eq. (3).

Additionally, the non-negligible influences from the high-temperature and high-velocity metal vapor are considered empirically in this model (Muhammad et al., 2018). These momentum and thermal factors include the stagnation pressure p_{vapor} and the shear stress τ_{vapor} from the impact of the high-velocity vapor on the keyhole surface, the additional heating effect from the vapor plume q_{plume} and the release of the evaporation latent heat due to the vapor's re-condensation q_{recond}.

3.3 Boundary Conditions

The thermal boundary condition on the keyhole wall, considering the energy balance between the laser energy, thermal loss, heating from the metal vapor as well as the energy transferred into the base metal, is given as:

$$k\frac{\partial T}{\partial \vec{n}} = q_{\mathrm{L}} - h_{\mathrm{c}}(T - T_0) - \sigma\varepsilon_{\mathrm{r}}(T^4 - T_0^4) - \rho v_{\mathrm{evp}}\Delta L_{\mathrm{v}} + q_{\mathrm{plume}} + q_{\mathrm{recond}} \quad (18)$$

The force balance on the keyhole wall in normal and tangential directions can be written as follows:

$$-p + 2\mu\frac{\partial v_{\mathrm{n}}}{\partial \vec{n}} = -p_{\mathrm{r}} - p_{\mathrm{vapor}} + p_{\mathrm{ca}} \quad (19)$$

$$-\mu\frac{\partial v_{\mathrm{t}}}{\partial \vec{n}} = \tau_{\mathrm{ma}} + \tau_{\mathrm{vapor}} \text{ . (20)}$$

3.4 Numerical Setup

The simulation domain has a dimension of 30 mm × 8 mm × 12 mm, including 10 mm of steel plate and 2 mm of Argon atmosphere above, see Fig. 4. To reduce the computational intensity, the central zone is finely meshed with hexahedron cells of 0.2 mm, and the cells grow coarser gradually in the outer zone. The physical properties of the materials are taken from the works of Su et al. (2005)

and Mills (2002). The specific heat, viscosity, thermal conductivity, surface tension coefficient and electric conductivity are temperature-dependent, whereby the remaining properties are constants.

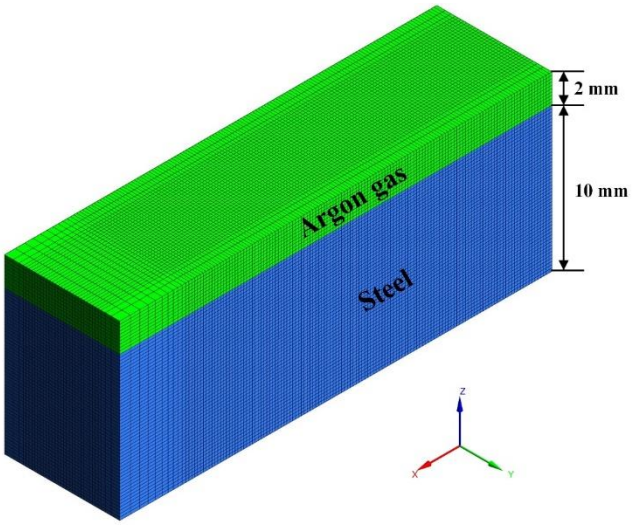

Fig. 4 Computational domain and mesh

The finite volume software ANSYS Fluent 19.2 was used to solve all transport equations. The second order upwind method was used for the spatial discretization of the convection-diffusion equations. The Pressure-Implicit with Splitting of Operators (PISO) algorithm was applied for the pressure-velocity coupling. The simulation was performed on a high-performance computing cluster. Sixty hours clock time were needed for 0.9 s real time welding process simulation when using 80 CPU cores and 128 GB RAM.

4. Results and discussion

4.1 Model validation

The experimental and the calculated weld geometries from three EMS-WFLBW cases with different magnetic field angles (10°, 20° and 40°) and one reference WFLBW case without EMS are given in Fig. 5. The red region represents the calculated weld zone, and the dashed line is the experimental boundary of the weld zone. The comparison shows a good agreement between the experimental and numerical results, which validates the creditability of the model. The detailed deviations between the experimental and numerical results are listed in Table 3.

It can be found experimentally that the magnetic field orientation shows a remarkable influence on the penetration depth. The traditional WFLBW gives the maximum penetration depth (7.5 mm), as shown in Fig. 5(a). As the magnetic field angle decreases from 40° to 10°, the penetration

depth decreases as well, from 6.9 mm to 5.9 mm. Overall, the introduction of the magnetic field brings a reduction in the penetration depth. It can be partially attributed to the enhancement of the Lorentz force on the upper keyhole collapse and the backward flow (Meng et al., 2019a), which is considered self-consistently in the model. Another possible reason is that the melting front of the filler wire is also affected by the oscillating magnetic field. The vibration of the melting front under the high-frequency Lorentz force may increase the dissipation ratio of the laser energy at the melting front. Since the solid filler wire is not built in the model, this influence must be involved empirically by adapting the blocked area in Fig. 3(a) through trial-and-error method to change the total laser energy efficiency, rather than self-consistently.

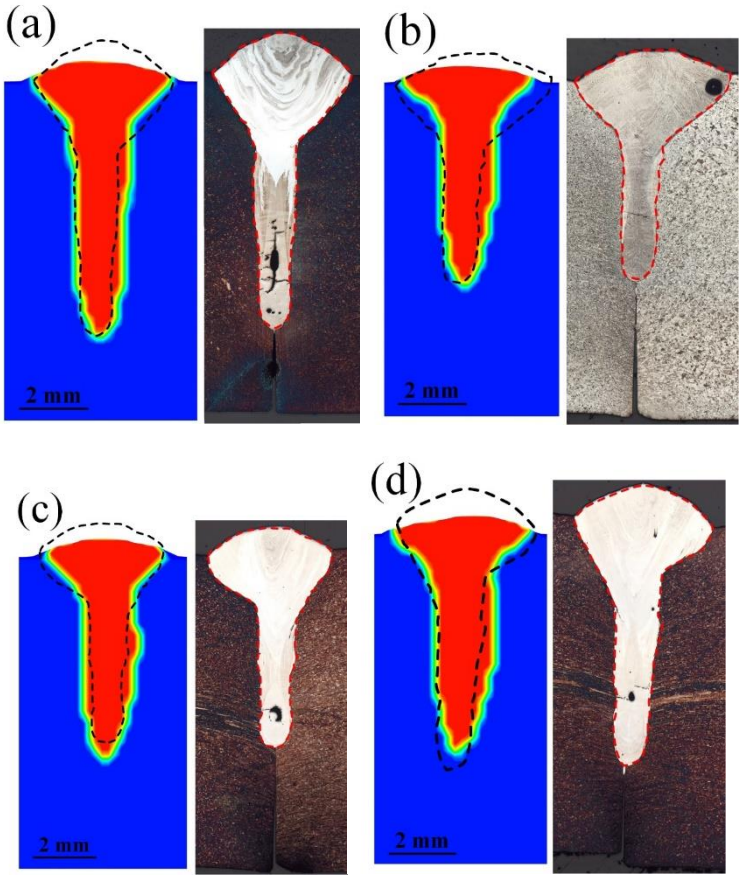

Fig. 5 Simulated and experimental weld cross-section: (a) reference case, (b) magnetic field of 10° angle, (c) magnetic field of 20° angle, (d) magnetic field of 40° angle

Table 3 Deviation between experimental and calculated penetration and weld width

Case	Penetration			Weld width		
	Exp. (mm)	Num. (mm)	Deviation	Exp. (mm)	Num. (mm)	Deviation
Reference	7.5	7.7	2.6%	4.1	4.3	4.9%

10° angle	5.9	6.2	5.1%	4.6	4.0	13.0%
20° angle	5.5	6.1	10.9%	3.6	3.7	2.8%
40° angle	6.9	6.5	-5.8%	4.1	4.2	2.4%

4.2 Electromagnetic behavior

The oscillating magnetic field induces an alternating current, namely eddy current, in the workpiece. Fig. 6 shows the vector field of the induced current density. The magnitude of the eddy current is highly dynamic due to the high frequency of the magnetic field thus it is normalized for a better visualization. Several common features can be found among these cases. There are two dominant circulating currents in the workpiece, and they are separated by the high-temperature and non-conducting keyhole. Depending on the temporal variation of the magnetic flux density, the circulating current can be either clockwise or counterclockwise. The maximum current density always appears in the cold metal part in front of the keyhole. The circulating current is quite regular in the cold metal part due to the homogenous electric conductivity there. In contrast, the current density in the molten pool is relatively irregular due to the inhomogeneous electric conductivity and the liquid movement. This distribution pattern of the induced current is consistent with the calculation results of the finite element model with a fixed keyhole from Bachmann et al. (2016).

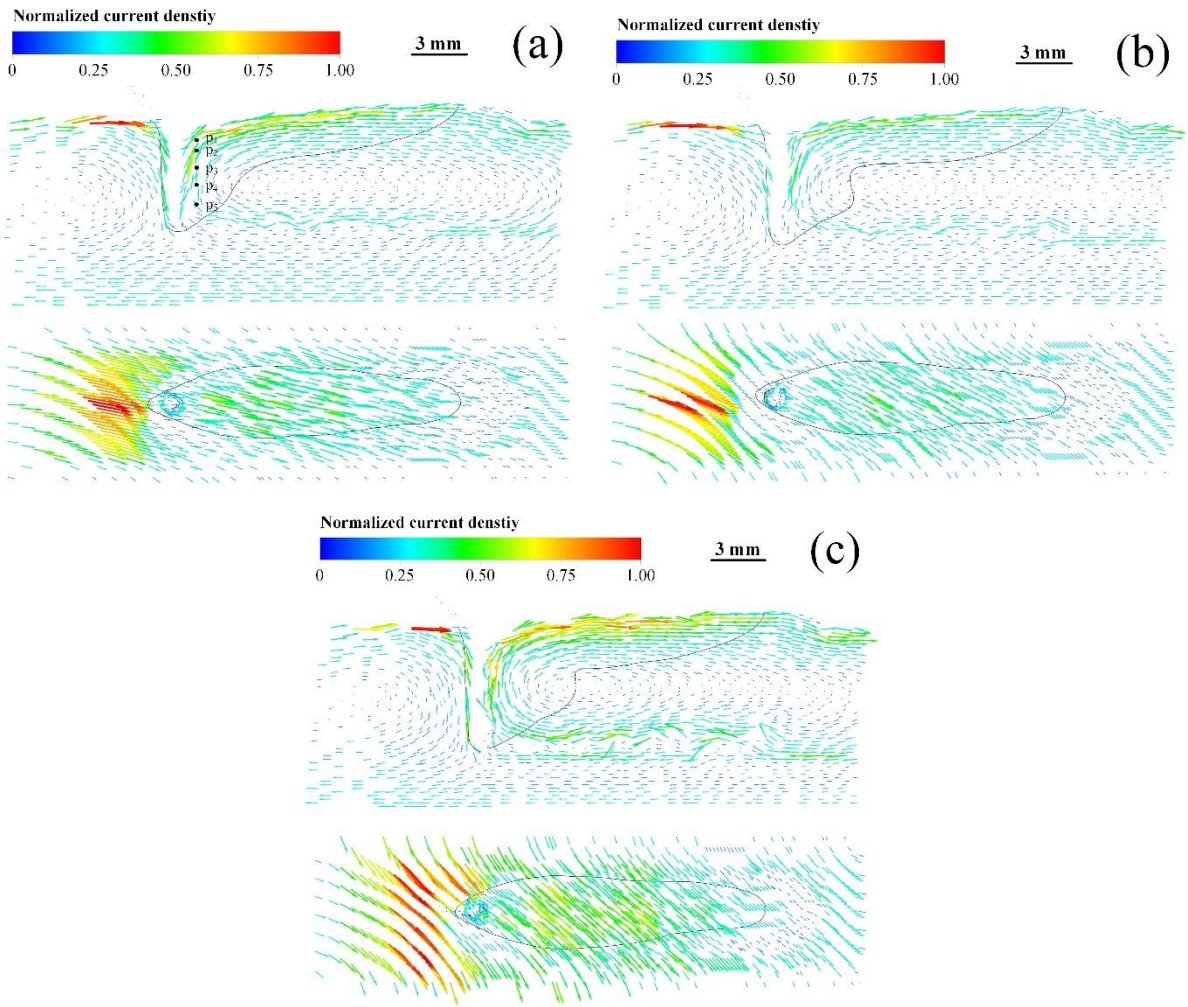

Fig. 6 Vector field of the induced eddy current: (a) magnetic field of 10° angle, (b) magnetic field of 20° angle, (c) magnetic field of 40° angle

Gatzen et al. (2011b) suggested that the direction of the induced current is mainly determined by the liquid flow under a steady or low-frequency magnetic field, see $\vec{v}\times\vec{B}$ term in Eq. (1), since the magnetic field has a defined direction. However, the induced circulating current is basically vertical to the direction of the magnetic field in Fig. 6, which obeys the Lenz's law. It means that temporal variation of the magnetic field ($\vec{E}$ term) rather than the Hartmann effect ($\vec{v}\times\vec{B}$ term) dominates the induced current in this study. As the magnetic field angle changes from 10° to 40°, the angle of the circulating current with respect to the *y*- axis varies from 80° to 50°.

The root mean square (RMS) value of the induced current density along the *z*-direction (line p_1p_5 in Fig. 6) is plotted in Fig. 7. The RMS values are calculated from 50 periods in each case. The magnetic field of 40° angle generates the strongest eddy current at the top region of the molten pool (7.7×10^6 A/m^2), and the local eddy current reduces to 6.4×10^6 A/m^2 as the angle reduces to 10°.

The difference in the current magnitude can be explained by the total electrical resistance along the route of the circulating current, as shown in Fig. 8. The molten pool gives a higher electrical resistance because the electrical resistivity of austenitic steel has a positive correlation with temperature. The eddy current produced by the magnetic field of 10° angle nearly flows along the longitudinal direction, therefore is confronted with higher electrical resistance along its route.

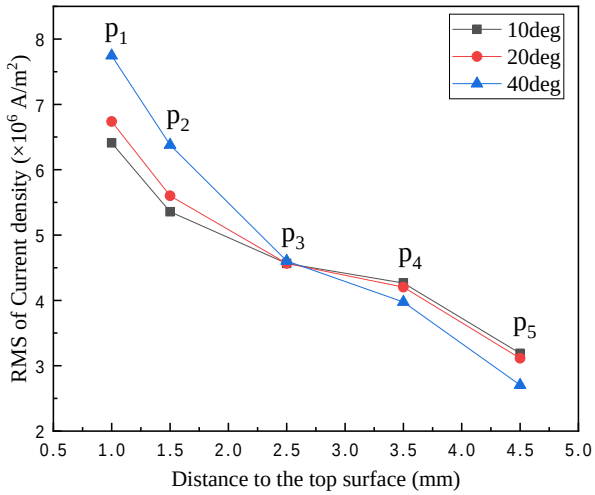

Fig. 7 RMS value of current density along *z*-direction

However, the eddy current produced by the magnetic field of 40° angle shows a faster decrement along the *z*-direction. It can be ascribed to the presence of the skin effect by which the alternating current tends to concentrate at the surface of a conductor. When an oscillating magnetic field is applied, the skin depth of the induced current can be estimated by the following equation:

$$\delta=\left(\pi f \mu_0 \sigma_e\right)^{-1/2} \quad . (21)$$

It shows clearly that the eddy current with a certain frequency has a smaller skin depth (worse penetration capacity) in a conductor with lower electrical resistivity (higher electrical conductivity). Since the induced current from the magnetic field of 40° angle confronts the lower electrical resistivity, it attenuates more significantly along the thickness direction.

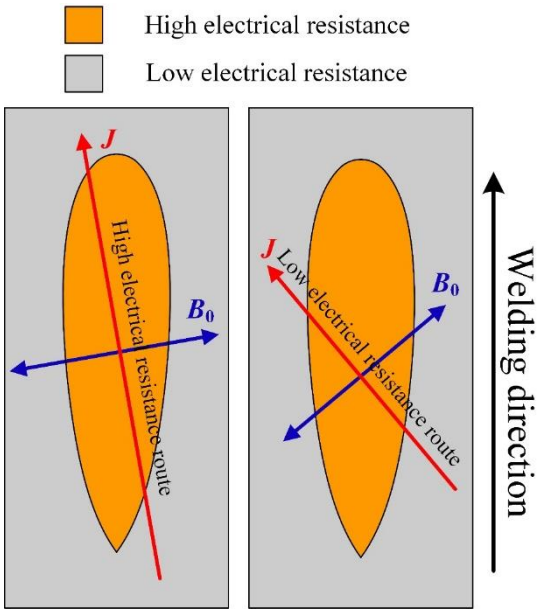

Fig. 8 Different electrical resistances along the current route

The magnitude of the Lorentz force and its three components long line p_1p_5 in Fig. 6 are given in Fig. 9. Corresponding to the induced current in Fig. 7, the magnitude of the Lorentz force also decreases along the z-direction, whereby this phenomenon limits the penetration capacity of the magnetic field. The case with magnetic field of 40° angle shows the fastest decrement. The Lorentz force in *z*-direction with an order of magnitude of 10^6 N/m^3 plays the dominant role at the top region of the molten pool in all three cases, as shown in Fig. 9(d). It decreases dramatically along the z-direction, remaining at its minimum around 1×10^5 N/m^3 at the bottom region.

Fig. 6 shows that the induced current turns from *x*-direction to *z*-direction as it approaches the keyhole region. Consequently, the Lorentz force in *x*-direction has a higher proportion at the lower region of the molten pool. It gives the strongest Lorentz force in *x*-direction when the magnetic field of 10° angle is applied. The *x* component of the Lorentz force increases first along the thickness direction to a peak value of 4.1×10^5 N/m^3 and decreases afterwards. A similar trend can also be found in the case with a magnetic field of 20° angle. The *x* component of the Lorentz force monotonically decreases along the thickness direction under magnetic field of 40° angle.

The magnetic field of 40° induces the strongest Lorentz force in *y*-direction, as shown in Fig. 9(c), whereas the magnetic field of 10° produces the smallest. It can be found by comparing Fig. 9(b)~(d) that the *y* component of the Lorentz force is relatively minor in all three cases.

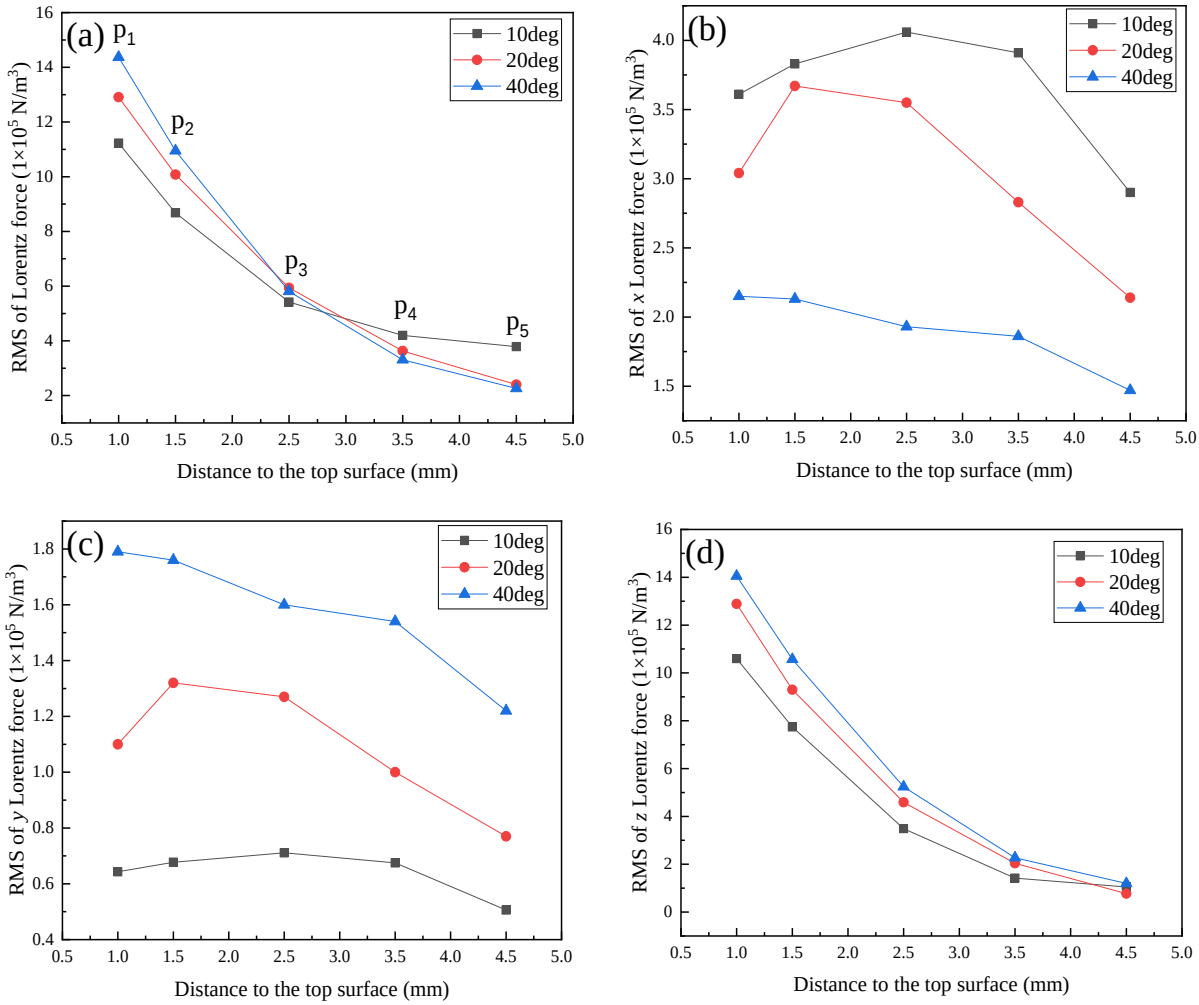

Fig. 9 RMS value of the Lorentz force along the thickness direction: (a) magnitude, (b) *x* component, (c) *y* component, (d) *z* component

4.3 Metal mixing and molten pool behavior

The XRF mappings of the Ni distribution on the cross-section are shown in Fig. 10(a). The Ni concentrates on the upper region of the weld in the reference case, implying an insufficient mixing during the welding process. Furthermore, the Ni-rich region and the Ni-poor region are sharply differentiated without any apparent transition region in between. When the magnetic field of 10° angle is applied, the filler metal can be transferred to the bottom region, and the Ni distributes homogeneously on the whole cross-section. The filler material can also reach the root of the weld by using a 20° magnetic field angle. However, the metal mixing in the bottom region is not as sufficient as in the case with magnetic field of 10° angle. In the case of 40° magnetic field angle, no apparent improvement in the mixing can be found, compared with the reference case. In summary, the mixing enhancement from the EMS becomes weaker as the magnetic field angle varying from 10° to 40°. The calculated results in Fig. 10 (b) show the same variation trend, and the Ni distribution pattern in

each case also has a good agreement with the experimental one. It further proves the reliability of the model.

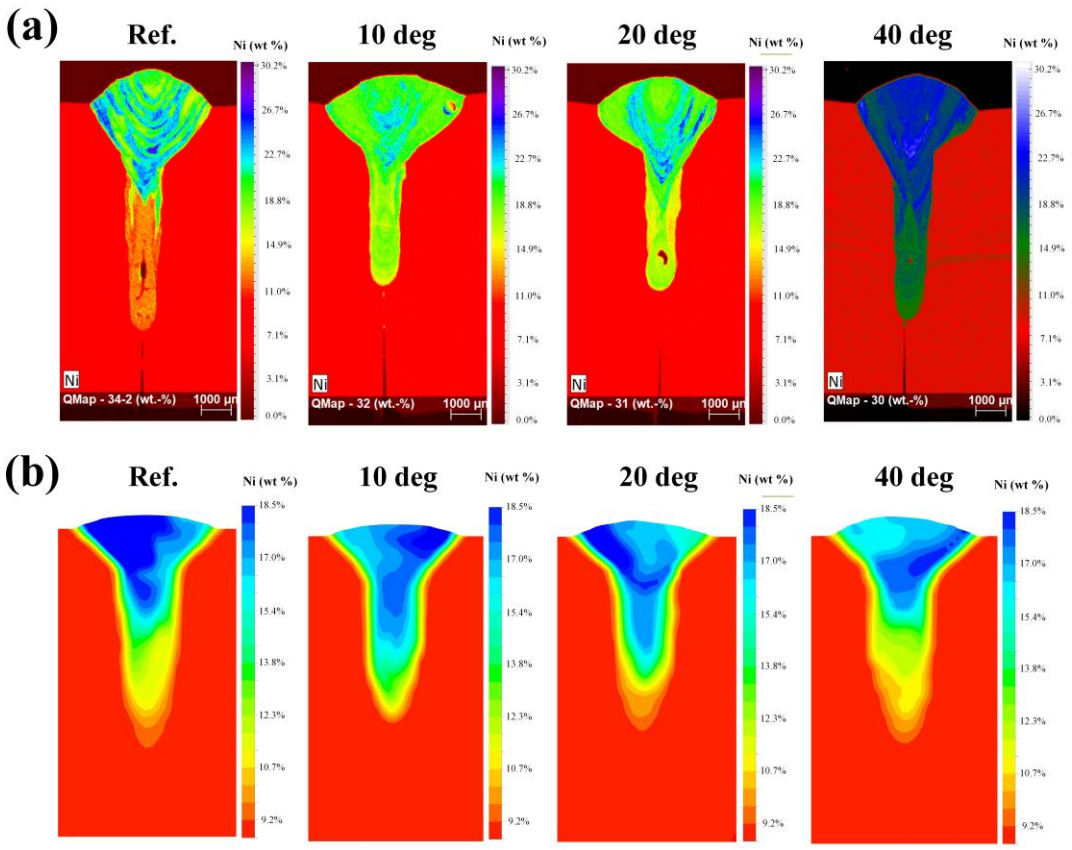

Fig. 10 Ni distribution (in wt.%) in the cross-section: (a) XRF measurement, (b) numerical results

Fig.11 gives the Ni distribution on the longitudinal section. In all cases, the melted filler metal impacts on the keyhole front wall first, but no noticeable downward transfer occurs along the keyhole front wall. It can be ascribed to the extremely thin liquid layer on the keyhole front wall and its fluctuating flow pattern (Zhou et al., 2016). At the initial stage, the filler metal is well mixed in the molten pool in all MHD cases. The initial molten pool with a smaller volume is effortlessly stirred by the Lorentz force. Moreover, the molten pool has a closely axisymmetric shape, rather than a typical tear-dropped shape, at the initial stage. The magnetic fields with different angles provide a similar penetration capacity because different circulating currents confront similar electrical resistances along their route. As the molten pool is elongated, spiking of Ni distribution can be found in the longitudinal section, especially for the cases with a magnetic field of 20° angle, despite the molten pool has reached the quasi-steady state. The highly dynamic keyhole fluctuation and molten pool flow contribute to these spiking phenomena. However, the spiking in Fig. 11(b) is much finer

compared to this in Fig. 11(c). It again verifies the better mixing enhancement from the magnetic field of 10° angle.

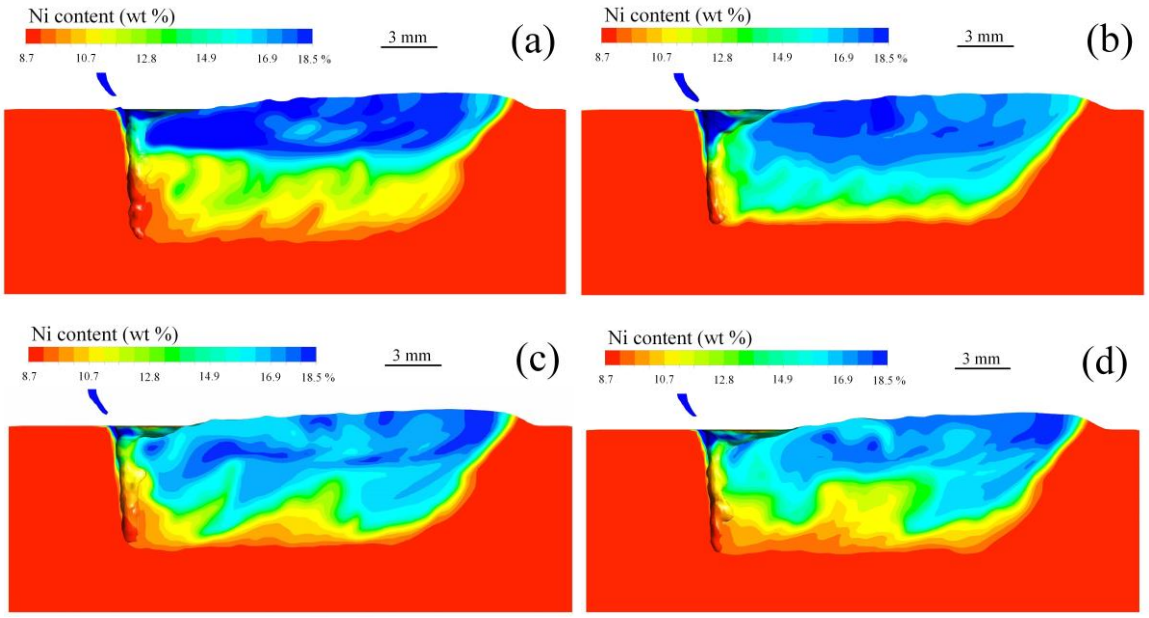

Fig. 11 Calculated Ni distribution (in wt.%) on the longitudinal section: (a) reference case, (b) magnetic field of 10° angle, (c) magnetic field of 20° angle, (d) magnetic field of 40° angle

Although the external magnetic field is applied, the basic flow pattern in all three MHD cases remains similar to the reference case. As shown schematically in Fig. 12, the melted metal flows around the keyhole and subsequently flows backward along the periphery of the molten pool. The liquid metal is redirected at the middle part of the molten pool and flows forward along the longitudinal plane. Although no further data are available from the open literature for WFLBW so far, this typical flow pattern has been affirmed both experimentally and numerically in HLAW with a leading arc by Cho et al. (2010) and Zhao et al. (2009), which has close physical essence with WFLBW. The transfer of the filler metal, especially along the *z*-direction, is predominantly determined by the flow pattern in the longitudinal plane, which will be emphatically discussed in the following part.

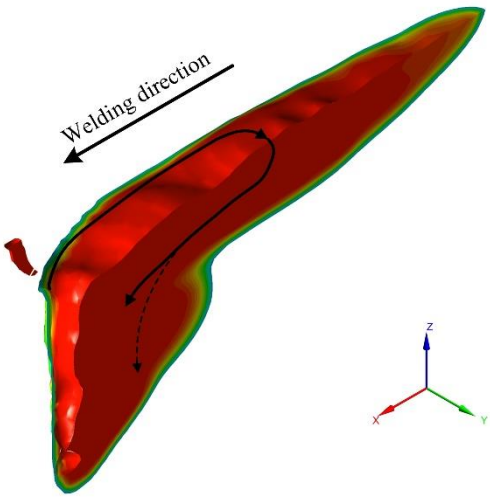

Fig. 12 Schematic of the fluid flow in the molten pool

Although a strong forward flow can be observed at the upper region of the molten pool in the reference case, no vigorous circulation forms at the lower region, as given in Fig. 13(b). There is almost no mass transfer between the Ni-rich region and the Ni-poor region, resulting into the sharp separation in Fig. 10 (a). Under the EMS from the magnetic field of 10° angle, a downward flow forms along the longitudinal section and correspondingly the filler metal is brought to the root of the molten pool. A similar flow pattern can be observed in the case with a magnetic field of 20° angle. It gives an explanation to the improved mixing in Fig. 10(b) and (c). In the 40° angle case, no apparent downward flow can be found, which restrains the Ni at the upper part of the molten pool.

The influence of the external magnetic field on the liquid metal flow results into a change of the molten pool shape. A bulging region forms in the reference case, as shown in Fig. 13(a). Recently, this unusual molten pool shape was found in autogenous LBW and it may initiate some defects, e.g. hot cracking (Wang et al., 2018). In this study, the bulging phenomenon narrows the metal transfer channel between the top and bottom regions and may further contribute to the filler metal concentration. When the magnetic fields of 10° and 20° angles are applied, the bulging is eliminated by the EMS, thus providing a downward transfer channel for the melt. In contrast, the magnetic field of 40° provides the weakest penetration capacity, see Fig.7, thus the bulging region remains.

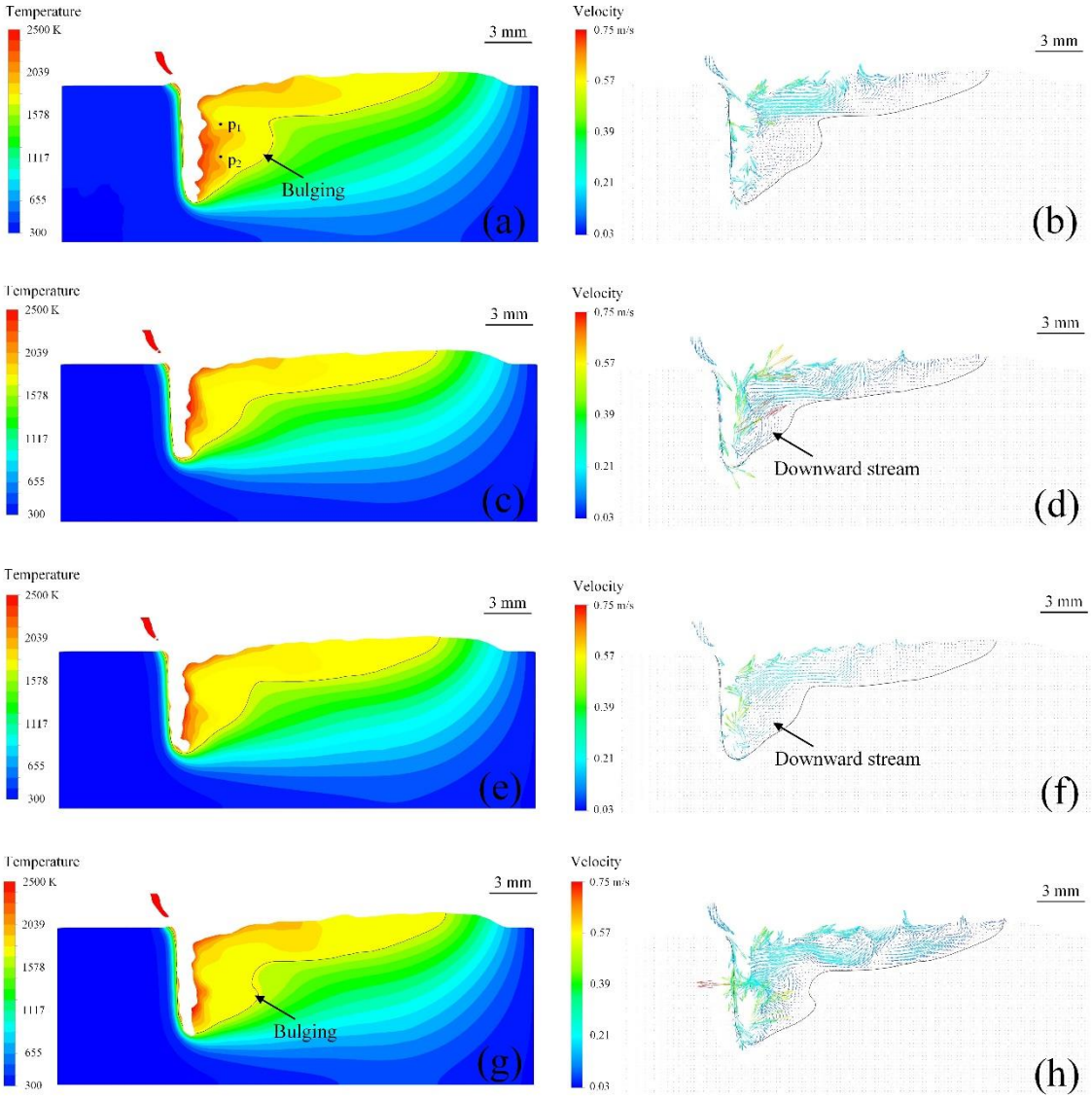

Fig. 13 Temperature distribution and velocity field of the molten pool: (a) and (b) for reference case, (c) and (d) for magnetic field of 10° angle, (e) and (f) for magnetic field of 20° angle, (g) and (h) for magnetic field of 40° angle

The time-velocity curves for two fixed points in the molten pool are plotted in Fig. 14. These two points are marked as p_1 (z=7.5 mm) and p_2 (z= 5.5 mm) in Fig. 13(a). Although the external magnetic field produces the strongest Lorentz force in the top region of the molten pool in all three cases, the variation of the magnetic field angle shows minor influence on the z component of the velocity. It indicates that the impact of the Lorentz force is covered by the strong momentum from the recoil pressure and the Marangoni stress. The variation of the magnetic field angle, however, shows considerable influence on the time-dependent velocity in z-direction in the lower region, which is highlighted by a dashed box in Fig. 14(b). Since the magnetic field of 10° angle gives the strongest

penetration capacity, the Lorentz force can reach deep regions of the molten pool, see Fig. 7 and Fig. 9(a). Therefore, a constantly downward flow with a magnitude of 0.05 m/s is formed. The velocity in *z*-direction fluctuates around zero due to the smaller Lorentz force produced by the magnetic field of 20° angle. An upward flow forms under the magnetic field of 40°, which is analogous to the flow pattern of the welding case without magnetic field (Meng et al., 2019b). Thus, there is evidence to suggest that the Lorentz force has attenuated to a minor level due to the stronger skin effect.

The different sizes of spiking in Fig. 11 can also be explained by the time-dependent *z* velocity in Fig. 14(b). The spiking phenomenon can be mitigated with either constantly downward or upward flow. When the *z*-direction of the flow varies rapidly, i.e. the *z* velocity fluctuates around zero, more apparent spiking will be formed.

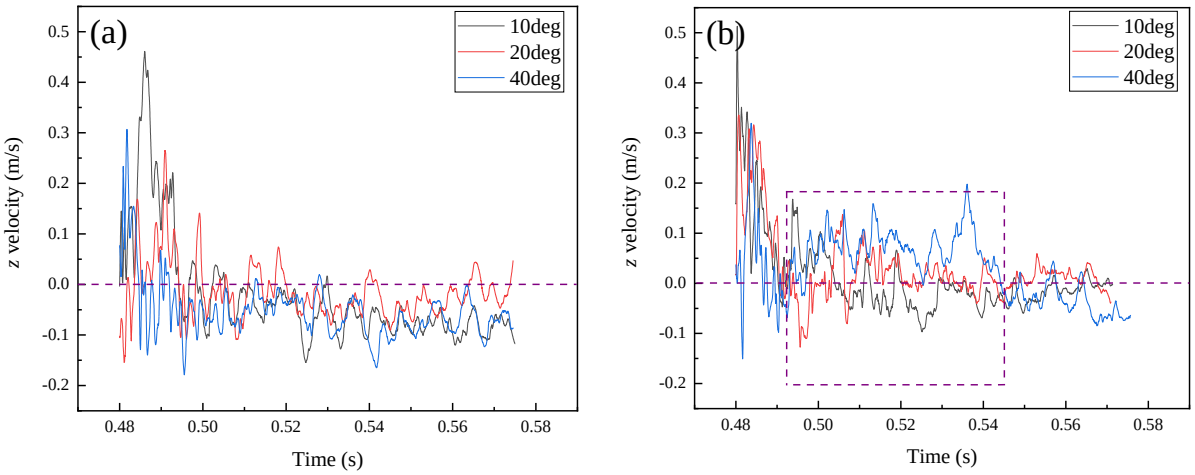

Fig. 14 Time-dependent *z* velocity on the longitudinal section (a) z=7.5 mm, (b) z=5.5 mm

5. Conclusions

In the current study, a combination of experimental investigation and multi-physical modelling is proposed to study the influence of the orientation of an oscillating magnetic field (magnetic field angle) on the metal mixing in the electromagnetic stirring enhanced wire feed laser beam welding. The main conclusions are drawn as following:

(1) The filler metal is distributed homogenously in the final weld under a magnetic field of 10° angle (with respect to the *y*-axis). The mixing enhancement attenuates as the magnetic field angle is increasing. No noticeable improvement of metal mixing can be observed when a magnetic field of 40° angle is applied.

(2) The magnetic field of 40° angle produces the highest induced eddy current at the top region of the molten pool and correspondingly the strongest Lorentz force. However, it shows the least penetration capacity due to the skin effect, which decreases the Lorentz force significantly along the thickness direction. As the magnetic field angle reduces from 40° to 10°, the penetration capacity of the magnetic field becomes stronger. Therefore, the EMS effect from the Lorentz force can reach the lower region of the molten pool.

(3) A constantly downward flow forms at the lower part of the molten pool under the EMS from a magnetic field of 10° angle, which contributes to a homogenous Ni distribution in the weld. With the magnetic angle increasing from 10° to 40°, the downward flow gradually turns into a constant upward flow, leading to insufficient mixing in the molten pool.

Acknowledgment

This work is funded by the Deutsche Forschungsgemeinschaft (DFG, German Research Foundation)—Project No. 416014189.

References

Arata, Y., Maruo, H., Miyamoto, I., Nishio. R., 1986. High Power CO_2 Laser Welding of Thick Plate: Multipass Weding with Filler Wire (Welding Physics, Process & Instrument). Transact JWRI 15, 199-206

Avilov, V., Fritzsche, A., Bachmann, M., Gumenyuk, A., Rethmeier, M., 2016. Full penetration laser beam welding of thick duplex steel plates with electromagnetic weld pool support. J. Laser Appl. 28, 022420.

Bachmann, M., Avilov, V., Gumenyuk, A., Rethmeier, M., 2014. Experimental and numerical investigation of an electromagnetic weld pool support system for high power laser beam welding of austenitic stainless steel. J. Mater. Process. Technol. 214, 578-591.

Bachmann, M., Kunze, R., Avilov, V., Rethmeier, M., 2016. Finite element modeling of an alternating current electromagnetic weld pool support in full penetration laser beam welding of thick duplex stainless steel plates. J. Laser Appl. 28, 022404.

Cao, L., Zhou, Q., Liu, H., Li, J., Wang, S., 2020. Mechanism investigation of the influence of the magnetic field on the molten pool behavior during laser welding of aluminum alloy. Int. J. Heat Mass Transf. 162, 120390.

Chen, J., Wei, Y., Zhan, X., Pan, P., 2017. Weld profile, microstructure, and mechanical property of laser-welded butt joints of 5A06 Al alloy with static magnetic field support. Int. J. Advanced Manu. Technol. 92, 677-1686.

Chen, J., Wei, Y., Zhan, X., Gao, Q., Zhang, D., Gao, X., 2018a. Influence of magnetic field orientation on molten pool dynamics during magnet-assisted laser butt welding of thick aluminum alloy plates. Opt. Laser Technol. 104, 148-158.

Chen, J., Wei, Y., Zhan, X., Gu, C., Zhao, X., 2018b. Thermoelectric currents and thermoelectric-magnetic effects in full-penetration laser beam welding of aluminum alloy with magnetic field support. Int. J. Heat Mass Transf. 127, 332-344.

Chen, R., Kong, H., Luan, J., Wang, A., Jiang, P., Liu, C., 2020. Effect of external applied magnetic field on microstructures and mechanical properties of laser welding joint of medium-Mn nanostructured steel. Mater. Sci. Eng.: A, 792, 139787.

Cho, W. I., Na, S. J., Cho, M. H., Lee, J. S., 2010. Numerical study of alloying element distribution in CO2 laser–GMA hybrid welding. Comput. Mater. Sci. 49, 792-800.

Cho, W. I., Na, S. J., Thomy, C., Vollertsen, F., 2012. Numerical simulation of molten pool dynamics in high power disk laser welding. J. Mater. Process. Technol. 212, 262-275.

Fritzsche, A., Hilgenberg, K., Teichmann, F., Pries, H., Dilger, K., Rethmeier, M., 2018. Improved degassing in laser beam welding of aluminum die casting by an electromagnetic field. J. Mater. Process. Technol. 253, 51-56.

Gatzen, M., Tang, Z., Vollertsen, F., 2011a. Effect of electromagnetic stirring on the element distribution in laser beam welding of aluminium with filler wire. Phys. Procedia 12, 56-65.

Gatzen, M., Tang, Z., Vollertsen, F., Mizutani, M., Katayama, S., 2011b. X-ray investigation of melt flow behavior under magnetic stirring regime in laser beam welding of aluminum. J. Laser Appl. 23, 032002.

Gatzen, M., Tang, Z., Vollertsen, F., Mizutani, M., Katayama, S., 2011c. X-ray investigation of melt flow behavior under magnetic stirring regime in laser beam welding of aluminum. J. Laser Appl. 23, 032002.

Gatzen, M., 2012. Influence of low-frequency magnetic fields during laser beam welding of aluminium with filler wire, Phys. Procedia 39, 59-66.

Hu, R., Luo, M., Liu, T., Liang, L., 2019. A. Huang, D. Trushnikov, S. Pang, Thermal fluid dynamics of liquid bridge transfer in laser wire deposition 3D printing. Sci. Technol. Weld. Join. 24, 401-411.

Kern, M., Berger, P., Huegel, H., 2000. Magneto-fluid dynamic control of seam quality in CO2 laser beam welding. Weld. J. 79, 72-78.

Meng, X., Bachmann, M., Artinov, A., Rethmeier, M., 2019a. Experimental and numerical assessment of weld pool behavior and final microstructure in wire feed laser beam welding with electromagnetic stirring. J. Manu. Process. 45, 408-418.

Meng, X., Artinov, A., Bachmann, M., Rethmeier, M., 2019b. Numerical and experimental investigation of thermo-fluid flow and element transport in electromagnetic stirring enhanced wire feed laser beam welding. Int. J. Heat Mass Transf. 144, 118663.

Meng, X., Artinov, A., Bachmann, M., Rethmeier, M., 2020. Theoretical study of influence of electromagnetic stirring on transport phenomena in wire feed laser beam welding. J. Laser Appl. 32, 022026.

Mills, K. C., 2002. Recommended values of thermophysical properties for selected commercial alloys, first ed., Woodhead Publishing, Cambridge.

Moreau, R. J., 2013 Magnetohydrodynamics, first ed., Springer Science & Business Media, Berlin.

Muhammad, S., Han, S. W., Na, S. J., Gumenyuk, A., Rethmeier, M., 2018. Study on the role of recondensation flux in high power laser welding by computational fluid dynamics simulations. J. Laser Appl. 30, 012013.

Rong, Y., Xu, J., Cao, H., Zheng, H., Huang, Y., Zhang, G., 2017. Influence of steady magnetic field on dynamic behavior mechanism in full penetration laser beam welding. J. Manu. Process. 26, 399-406.

Schulz, W., Simon, G., Urbassek, H. M., Decker, I., 1987. On laser fusion cutting of metals. J. Phys. D-Appl. Phys. 20, 481-488.

Semak, V., Matsunawa, A., 1997. The role of recoil pressure in energy balance during laser materials processing. J. Phys. D-Appl. Phys. 30, 2541.

Su, Y., Li, Z., Mills, K. C., 2005. Equation to estimate the surface tensions of stainless steels. J. Mater. Sci. 40, 2201–2205.

Torkamany, M. J., Kaplan, A. F., Ghaini, F. M., Vänskä, M., Salminen, A., Fahlström, K., Hedegård, J., 2015. Wire deposition by a laser-induced boiling front. Opt. Laser Technol. 69, 104-112.

Üstündağ, Ö., Avilov, V., Gumenyuk, A., Rethmeier, M., 2019. Improvement of filler wire dilution using external oscillating magnetic field at full penetration hybrid laser-arc welding of thick materials. Metals, 9, 594.

Wang, H., Nakanishi, M., Kawahito, Y., 2018. Dynamic balance of heat and mass in high power density laser welding. Opt. Express 26, 6392-6399.

Xu, L., Tang, X., Zhang, R., Lu, F., Cui, H., 2020. Weld bead characteristics for full-penetration laser welding of aluminum alloy under electromagnetic field support. J. Mater. Process. Technol. 288, 116896.

Zhao, L., Sugino, T., Arakane, G., Tsukamoto, S., 2009. Influence of welding parameters on distribution of wire feeding elements in CO2 laser GMA hybrid welding. Sci. Technol. Weld. Join. 14, 457-467.

Zou, J. L., Wu, S. K., Yang, W. X., He, Y., Xiao, R. S., 2016. A novel method for observing the micro-morphology of keyhole wall during high-power fiber laser welding, Mater. Des. 89, 785-790.

Figure captions

Fig. 1 EMS-WFLBW experiment system: (a) experimental setup, (b) schematic of the magnetic field orientation

Fig. 2 Experimentally measured external magnetic field $\vec{B}_0$

Fig. 3 Ray tracing algorithm: (a) discretization of the laser beam energy; (b) multiple reflections on the keyhole wall

Fig. 4 Computational domain and mesh

Fig. 5 Simulated and experimental weld cross-section: (a) reference case, (b) magnetic field of 10° angle, (c) magnetic field of 20° angle, (d) magnetic field of 40° angle

Fig. 6 Vector field of the induced eddy current: (a) magnetic field of 10° angle, (b) magnetic field of 20° angle, (c) magnetic field of 40° angle

Fig. 7 RMS value of current density along *z*-direction

Fig. 8 Different electrical resistances along the current route

Fig. 9 RMS value of the Lorentz force along the thickness direction: (a) magnitude, (b) *x* component, (c) *y* component, (d) *z* component

Fig. 10 Ni distribution (in wt.%) in the cross-section: (a) XRF measurement, (b) numerical results

Fig. 11 Calculated Ni distribution (in wt.%) on the longitudinal section: (a) reference case, (b) magnetic field of 10° angle, (c) magnetic field of 20° angle, (d) magnetic field of 40° angle

Fig. 12 Schematic of the fluid flow in the molten pool

Fig. 13 Temperature distribution and velocity field of the molten pool: (a) and (b) for reference case, (c) and (d) for magnetic field of 10° angle, (e) and (f) for magnetic field of 20° angle, (g) and (h) for magnetic field of 40° angle

Fig. 14 Time-dependent *z* velocity on the longitudinal section (a) z=7.5 mm, (b) z=5.5 mm

Table captions

Table 1 Nominal composition of 304 steel and NiCr20Mo15 alloy (wt.%)

Table 2 Nomenclatures

Table 3 Deviation between experimental and calculated penetration and weld width